Damages induced by synchrotron radiation-based X-ray microanalysis in chrome yellow paints and related Cr-compounds : assessment, quantification, and mitigation strategies

Damages induced by synchrotron radiation-based X-ray microanalysis in chrome yellow paints and related Cr-compounds: assessment, quantification and mitigation strategies

Letizia Monico,[1,2,3,] Marine Cotte,[4,5] Frederik Vanmeert,[3,6] Lucia Amidani,[4,7] Koen Janssens,[3,8] Gert Nuyts,[3] Jan Garrevoet,[9] Gerald Falkenberg,[9] Pieter Glatzel,[4] Aldo Romani,[1,2] Costanza Miliani[10]*

[1] *CNR-SCITEC, via Elce di Sotto 8, 06123 Perugia (Italy)*

[2] *SMAArt Centre and Department of Chemistry, Biology and Biotechnology, University of Perugia, via Elce di Sotto 8, 06123 Perugia (Italy)*

[3] *AXES Research Group, NANOlab Centre of Excellence, University of Antwerp, Groenenborgerlaan 171, 2020 Antwerp (Belgium)*

[4] *ESRF, 71 avenue des martyrs, 38000 Grenoble (France)*

[5] *LAMS, CNRS UMR 8220, Sorbonne Université, UPMC Univ Paris 06, 4 place Jussieu 75005, Paris (France)*

[6] *Laboratories of the Royal Institute of Cultural Heritage (KIK-IRPA), Parc du Cinquantenaire 1, 1000 Bruxelles (Belgium)*

[7] *Rossendorf Beamline at the ESRF, HZDR, Institute of Resource Ecology, Dresden 01314, (Germany)*

[8] *Rijksmuseum, Conservation & Restoration—Scientific Research, Hobbemastraat 22, 1071 ZC Amsterdam (The Netherlands)*

[9] *DESY, Notkestraße 85, 22607 Hamburg (Germany)*

[10] *CNR-ISPC, via Cardinale Guglielmo Sanfelice 8, 80134 Napoli (Italy)*

email: letizia.monico@cnr.it

Abstract

Synchrotron radiation (SR)-based X-ray methods are powerful analytical tools for several purposes. They are widely used to probe the degradation mechanisms of inorganic artists' pigments in paintings, including chrome yellows ($PbCr_{1-x}S_xO_4$; $0 \leq x \leq 0.8$), a class of compounds often found in Van Gogh masterpieces.

However, the high intensity and brightness of SR beams raise important issues regarding potential damage inflicted on the analyzed samples. A thorough knowledge of the SR X-ray sensitivity of each class of pigment in the painting matrix is therefore required to find analytical strategies that seek to minimize the damage for preserving the integrity of the analyzed samples and to avoid data misinterpretation.

Here, we employ a combination of Cr K-edge X-ray absorption near edge structure (XANES) spectroscopy, Cr-K_β X-ray emission spectroscopy (XES) and X-ray diffraction (XRD) to monitor and quantify the effects of SR X-rays on the stability of chrome yellows and related Cr-compounds and to define mitigation strategies.

We found that the SR X-ray beam exposure induces changes in the oxidation state and local coordination environment of Cr-ions and leads to a loss of the compound's crystalline structure. The extent of X-ray damage depends on some intrinsic properties of the samples (chemical composition of the pigment as well as the presence/absence and nature of the binder). It can be minimized by optimizing the overall fluence/dose released to the samples and by working in vacuum and under cryogenic conditions.

1. Introduction

The use of synchrotron radiation (SR)-based X-ray methods to study cultural heritage objects has seen a considerable increase over the last two decades due to their capabilities to provide spatially resolved elemental, molecular and structural speciation down to the submicrometer scale.[1,2] In such context, X-ray diffraction (XRD), X-ray fluorescence (XRF) and X-ray absorption near edge structure (XANES) spectroscopy are considered non-destructive techniques and they are widely exploited to unveil the composition and degradation mechanisms of a number of constituents found in different kinds of artefacts.[1,2,3,4]

However, SR beams are orders of magnitude more intense and brighter than those produced by means of conventional laboratory sources, with fluences that tipically achieves values of ~10^8-10^{11} ph/μm^2.[5] This aspect raises important issues regarding potential damage of the analyzed objects/samples. Thus, understanding the nature and magnitude of the damage induced by SR X-rays and defining analytical strategies to mitigate it, is of great importance to preserve sample integrity and to avoid misinterpretation of data.

Irreversible changes were observed for some inorganic pigments, including Prussian blue ($MFe^{III}[Fe^{II}(CN)_6]\cdot xH_2O$; $M=K^+$, NH_4^+, Na^+)[6,7,8] and ultramarine blue [approximated as $(NaCa)_8[Al_6Si_6O_{24}](SO_4,S,Cl)_2$].[9,10] In the case of Prussian blue, it was found that SR used for Fe K-edge XANES investigations may cause the fading of the pigment, by inducing a conversion from Fe^{III} to Fe^{II}. The extent of the damage depends on several factors, such as the nature of the substrate, the sample conditioning and the SR doses employed during measurements.[6-8] For a series of natural and synthetic ultramarine blue pigments, changes in the S K-edge XANES spectra revealed that the prolonged exposure to a SR X-ray beam (with doses greater than ~10^2 MGy) promotes a redox process that leads to the transformation of polysulfides (more likely $[S_6]^{-2}$ and $[S_8]^{-2}$) into $S_3^{-\bullet}$ radicals. A level of damage of 10% or below was achieved using doses smaller than ~80 MGy.[9] For micro-

samples taken from discolored ultramarine areas of early 20th century oil paintings, comparison of light microscopy images before and after Al K-edge XANES investigations showed a darkening of the surface which, whilst not affecting the features of the XANES spectra, should be considered if samples are to be used for further analysis.[10]

SR-based X-ray methods were successfully employed for elucidating the degradation mechanisms of other inorganic pigments in oil paintings, such as vermilion (HgS),[11] red lead (Pb_3O_4),[12] cadmium yellows ($Cd_{1-x}Zn_xS$; $0 \leq x \leq 0.3$),[13,14,15,16,17,18] orpiment/realgar (arsenic sulfides),[19,20,21,22] zinc yellows ($K_2O \cdot 4ZnCrO_4 \cdot 3H_2O$),[23] and chrome yellows ($PbCr_{1-x}S_xO_4$; $0 \leq x \leq 0.8$).[24,25,26,27,28,29,30] However, a thorough knowledge of their sensitivity towards X-ray exposure is still lacking.

Here, we discuss the impact of monochromatic SR X-ray macro-/micro-beams on the stability of chrome yellow pigments and paints and we define a safe analytical protocol for their analysis. Chrome yellows are known for their tendency to undergo darkening when exposed to UVA-visible light.[24,31] By using SR-based Cr K-edge XANES in combination with electron paramagnetic resonance spectroscopy, we established that the darkening of chrome yellows in a number of Van Gogh paintings and artificially aged mock-ups is due to the photoreduction of the original Cr^{VI} to Cr^{III}-species (i.e., oxides and/or different organo-Cr^{III}-compounds), with Cr^{V}-species arising from the interaction between the pigment and the binder.[24-28,31,32,33] We also proved that Cr-reduction is favored by the presence of the binder;, it is stronger in $PbCr_{1-x}S_xO_4$ solid solutions ($0<x\leq0.8$) with respect to monoclinic $PbCrO_4$ and depends on the environmental conditions to which the pigment is exposed to.[29,31-33] Notably, we found that high moisture conditions promote the formation of higher amount of Cr^{V}-species, in contrast to the exposure to white light that favors the production of Cr^{III}-species.[32] Moreover, upon irradiation with different types of monochromatic light, at least two degradation pathways might have taken place, favoring the formation of different Cr^{III}-compounds. Cr^{III}-oxides are more likely to be present in paints aged at $\lambda \leq 450$ nm while

organo-Cr^{III}-compounds (e.g., acetate hydroxide, acetylacetonate) are encountered in the samples irradiated at λ≥500 nm.[31]

In this work, we focus on the SR X-ray stability of a set of Cr^{III}/Cr^{V}-compounds and two chrome yellow types: (a) monoclinic $PbCrO_4$ and (b) mainly orthorhombic $PbCr_{0.2}S_{0.8}O_4$ (i.e. pigments with properties similar to those identified in paintings).[34] The chrome yellows were investigated in the absence and presence of two binders: linseed oil and a water-based acrylic emulsion. Although the former is mainly used with chrome yellows by 19^{th}-20^{th} century painters,[26,35] the two binders were chosen due to their different contribution on the Cr^{VI}-reduction, being more significant when the pigment is mixed with linseed oil rather than with acrylic binder.[33]

By combining SR-based Cr K-edge XANES spectroscopy, Cr-K_β X-ray emission spectroscopy (XES) and μ-XRD we obtained semi-quantitative information about Cr-speciation changes induced by SR X-ray exposure and we correlated them to intrinsic properties of the samples and to a number of experimental parameters (such as. fluence/absorbed dose, ambient pressure and temperature). After discussing the results obtained and describing how they may introduce data misinterpretation in the study of the degradation of chrome yellows, we present experimental strategies to mitigate the SR X-ray-induced damage for this class of pigments.

2. Experimental section

2.1. Materials

2.1.1 Reference compounds. The following Cr-powders were analyzed: lead chromate ($PbCrO_4$, henceforth: CY_0 and sulfur-rich lead chromate ($PbCr_{0.2}S_{0.8}O_4$; henceforth: $CY_{0.8}$ which are yellow pigments synthetized in our laboratory (for further information see ref [34]). Cr^{III}-oxide (Cr_2O_3), Cr^{III}-acetylacetonate [$Cr(C_5H_7O_2)_3$], Cr^{III}-acetate hydroxide [$(CH_3CO_2)_7Cr_3(OH)_2$], sodium bis(2-hydroxy-2 methylbutyrato)-oxochromate(V) [$NaCrO_5(C_5H_8O)_2$; hereafter denoted "Na-oxochromate(V)"] (Sigma-Aldrich), Cr^{III}-hydroxide [$Cr(OH)_3$], Cr^{III}-oxalate [$Cr_2(C_2O_4)_3$] (City Chemical LLC), which are instead compounds selected based on previous studies,[24-29,31-33] being the most likely degradation products of chrome yellow paints.

For experiments at beamlines ESRF-ID21 and DESY-P06, finely milled powders were prepared as a thin layer fixed onto adhesive tape; for measurements at beamline ESRF-ID26, the powders were investigated as pellets (13 mm diameter) diluted with boron nitride. Powder compositions were preliminary checked by X-ray and vibrational spectroscopy methods.[24,34]

2.1.2 Paint mock-ups. Paint samples (~200-300 μm thickness) were prepared on polycarbonate slices using finely milled powders of either monoclinic $PbCrO_4$ or mainly orthorhombic $PbCr_{0.2}S_{0.8}O_4$ in mixture with either one of the following binders in a 4:1 weight ratio: linseed oil (Zecchi) or Primal B60-A (CTS Europe) (henceforward denoted "acrylic"). All paints were left to dry in the dark at 25-35°C temperature and 35-45% relative humidity (i.e., indoor temperature and humidity measured by a thermohygrometer) for ~3 months and then directly analyzed without any additional preparation.

2.2 Analytical methods

2.2.1 μ-XRF and μ-XANES at Cr K-edge. Measurements were performed at the scanning X-ray micro-spectroscopy end-station of beamline ID21 of the European Synchrotron Radiation Facility (ESRF, Grenoble).[36] A Si(220) double-crystal monochromator was used to scan the X-ray beam energy across the Cr K-edge (5.97–6.10 keV). For the calibration, the first inflection point of the first-order derivative Cr K-edge XANES spectrum of a Cr metallic foil was set at 5.9892 keV. A photon flux between 2×10^8 ph/s and 1×10^{10} ph/s (varied using Al attenuators of 20-100 μm thickness) was employed during the experiment. At the exit of the monochromator, the beam size was defined using pinholes (50-100 μm diameter) for macro-XANES characterization. In these conditions, the fluence rate was ~10^5-10^6 ph/s·μm^2. For μ-XANES investigations, the incident beam was focused with a Kirkpatrick-Baez (KB) mirror system down to a spot size of ~1.0×0.3 μm^2 (h×v). In these conditions, without beam attenuation, the fluence rate is typically ~10^{10} ph/s·μm^2. For normalization purposes, a photodiode upstream the sample is constantly monitoring the beam intensity.

XRF mapping was performed *via* raster-scanning of the samples with 100 ms/pixel dwell times and using a 80 mm^2 collimated active area silicon drift diode detector (Xflash 5100, Bruker). The PyMca software[37] was used to obtain the elemental and Cr-oxidation state maps (see SI for details).

For each sample an unexposed spot was selected and a series of XRF-mode XANES spectra was acquired there to follow the spectral evolution as a function of the fluence (ph/μm^2) and absorbed dose (MGy). Notably, in the case of paint mock-ups, the absorbed dose was calculated without considering the presence of the binder (see SI and Figure S1 for details). The acquisition time was 75 s per spectrum. Measurements were performed under vacuum (10^{-4}-10^{-5} mbar) both at room and cryogenic temperatures (sample stage cooled down to ~-150 °C by conductive Cu braids connected to a LN_2 filled Dewar).[38] The

ATHENA software[39] was used for normalization and for linear combination fitting (LCF) of the spectra using a library of Cr-references spectra (see SI for details).

2.2.2 Cr-K_β XES and Cr K-edge high-energy resolution fluorescence detected (HERFD)-XANES. Investigations were performed at beamline ID26 of the ESRF. The incident energy was selected using a Si(311) double-crystal monochromator. The emission spectrometer based on Rowland geometry was equipped with four spherically bent Ge(333) crystal analyzers (R=1000 mm). A Cr metallic foil was used to calibrate the incident energy, performed by setting the first inflection point of the first-order derivative to 5.989 keV. Samples were investigated in a fluorescence geometry oriented at 45° with respect to both the incident beam and the central analyzer crystal. The beam footprint size on the sample, determined by a pair of slits close to the sample, was 0.15 mm vertically and either 0.707 mm (slits at 0.5 mm) or 0.99 mm (slits at 0.7 mm) horizontally. The total flux varied from 1×10^{10} to 4×10^{12} ph/s, depending on the slit size and the presence of attenuators of different thickness (Figure S2).

XES measurements were performed with a 6.1 keV incident energy using two modalities: i) recording the full spectrum at a single point; ii) collecting each energy point of the spectrum at a different sample spot. The spectra acquired with mode ii) were also corrected for Cr concentration inhomogeneities. The second mode was implemented to minimize the fluence to the sample, thus any possible spectral changes due to X-ray exposure. The integration time per point was adapted to the Cr-concentration and the sensitivity of the sample towards X-rays. For sake of clarity, mode i) and ii) are henceforth denoted “high-fluence” and “low-fluence” modes, respectively.

The K_β main line spectra were recorded in the 5.91-5.96 keV range, with 0.2 eV energy increments and 2-7 s/point exposure time (total acquisition time for “high-fluence” spectra: ~250-1740 s). The profiles of K_β satellite lines were measured in the 5.951-6.021 keV range,

with energy step sizes of 1-0.3 eV and 1-14 s/point exposure time (total acquisition time for "high-fluence" spectra: ~390-2180 s).

To set the integration time per point needed to record XES spectra (in "low-fluence" mode) with minimum damage, a series of Cr K-edge HERFD-XANES spectra were acquired at an unexposed spot of the sample. The irradiation time before observing damage on HERFD-XANES was then taken as the total scanning time for XES. HERFD-XANES were also acquired before and after XES in "high-fluence mode" to evaluate the damage induced by the XES scan.

XES data were processed using PyMca.[37] The normalization and LCF of the XANES spectra was performed *via* ATHENA.[39]

2.2.3 μ-XRD. Investigations were carried out at beamline P06 of PETRA-III (DESY, Hamburg).[40] KB-mirrors were used to focus the primary beam of 21 keV to a spot of 0.65×0.75 μm^2 (v×h) and a flux of ~2×10^{10} ph/s. Diffraction patterns were collected by a PILATUS 300K area detector (Dectris Ltd., CH), positioned at *ca.* 140 mm behind the sample to capture d-spacing values between 1.4–20 nm (Q-values between 3–45 nm^{-1}). Calibration was performed by analyzing a LaB_6 reference.

A series of diffraction patterns were collected each second, while exposing the same spot to the X-ray beam for a period of 600 s or 1800 s. Azimuthal integration of the 2D diffraction images and data fitting was performed using the XRDUA software.[41] All non-overlapping diffraction signals with d-spacing values between 1.4–10 nm as well as a broad band (Q = 19.5 nm^{-1}) were fitted with Gaussian profiles. For each compound, the sum of these integrated (diffraction) peak intensities was monitored during irradiation. The background was modelled using a stripping function.

3. Results and Discussion

3.1 Cr-powders: nature of the SR X-ray-induced damage

To evaluate the effects of SR X-rays on different Cr-compounds, we started with the analysis of a set of Cr-powders (i.e. not mixed with the binder) on which a series of Cr K-edge XANES spectra at increasing fluences on a selected sample spot were recorded. XANES was chosen as primary monitoring method for its high sensitivity to the oxidation states and the local coordination environment of Cr-ions.[24,42,43,44,45]

The pre-edge structures are attributed to transitions from the Cr 1s orbital into orbitals with Cr 3d character. In octahedral Cr^{III}-compounds (Figure 1a-e: peaks A,B), orbitals with metal p and d character cannot mix due to symmetry inversion and the spectral intensity arises from quadrupole transitions resulting in weak pre-edge peaks (t_{2g} and e_g symmetry) at 5.9906 and 5.9931 keV. For tetrahedral Cr^{V}- and Cr^{VI}-compounds (Figure 1f-h: peak C), the pre-edge gains intensity from dipole-allowed transitions because orbitals with p and d symmetry can mix, appearing as a single peak (t_2 symmetry) of variable intensity at 5.9926 and 5.9931 keV, respectively. Differences in the features of the post-edge absorption region reflect the different Cr local environments in the respective crystal structures.[42-45]

Regarding the effects of SR X-rays on Cr^{III}-compounds, fluences in the 1.7×10^{7}-1.0×10^{13} ph/μm^2 range (~0.4–3×10^{5} MGy) do not induce any significant change in the XANES spectra of Cr_2O_3 and $Cr(OH)_3$ (Figure 1a,b). Small spectral differences in the post-edge absorption region are due to normalization. Meaningful modifications occur instead in the profiles of organo-Cr^{III} complexes starting from ~1.7×10^{8} ph/μm^2 (~1-2 MGy) (Figure 1c-e: red line). For such compounds, the shift of the absorption edge position towards lower energies (~1-2 eV) is clearly visible along with gradual disappearing of the pre-edge peak at 5.9931 keV. For Cr^{III}-acetylacetonate and Cr^{III}-oxalate a loss of structure and broadening of the post-edge features is visible too (Figure 1d,e). Such changes point out that exposure to SR X-rays induces modifications to the Cr^{III}-ions local coordination environment, possibly caused

by variations of the structure of ligands and/or weakening/breaking of the Cr^{III}-ligand bond.[42,43,45]

In line with the literature,[46] the Cr^{V}-compound Na-oxochromate shows a significant sensitivity under the SR X-ray beam exposure (Figure 1f). For fluences greater than 1.7×10^{7} ph/μm^2 (~0.1 MGy), the reduction of Cr^{V} to Cr^{III}-compounds is revealed by the shift of the absorption edge towards lower energies (~1 eV) and the progressive decrease of the intensity ratio between the bands at 5.9926 and 5.9906 keV (characteristic for Cr^{V} and Cr^{III}-species, respectively). Under comparable fluences, similar but less pronounced changes are observable in the XANES profiles of CrY_0 and $CrY_{0.8}$ powders (Figure 1g,h). With increasing fluences up to 1.0×10^{13} ph/μm^2 (~4×10^{5} MGy), the partial conversion of Cr^{VI} to Cr^{III}-species is pointed out by the gradual decreasing of the pre-edge peak intensity (quantitatively proportional to the Cr^{VI} to total Cr content ratio)[25,31] for both $CrY_{0.8}$ (15%) and CrY_0 (10%) (purple line) and by a small shift of the absorption edge energy (~-0.3 eV).

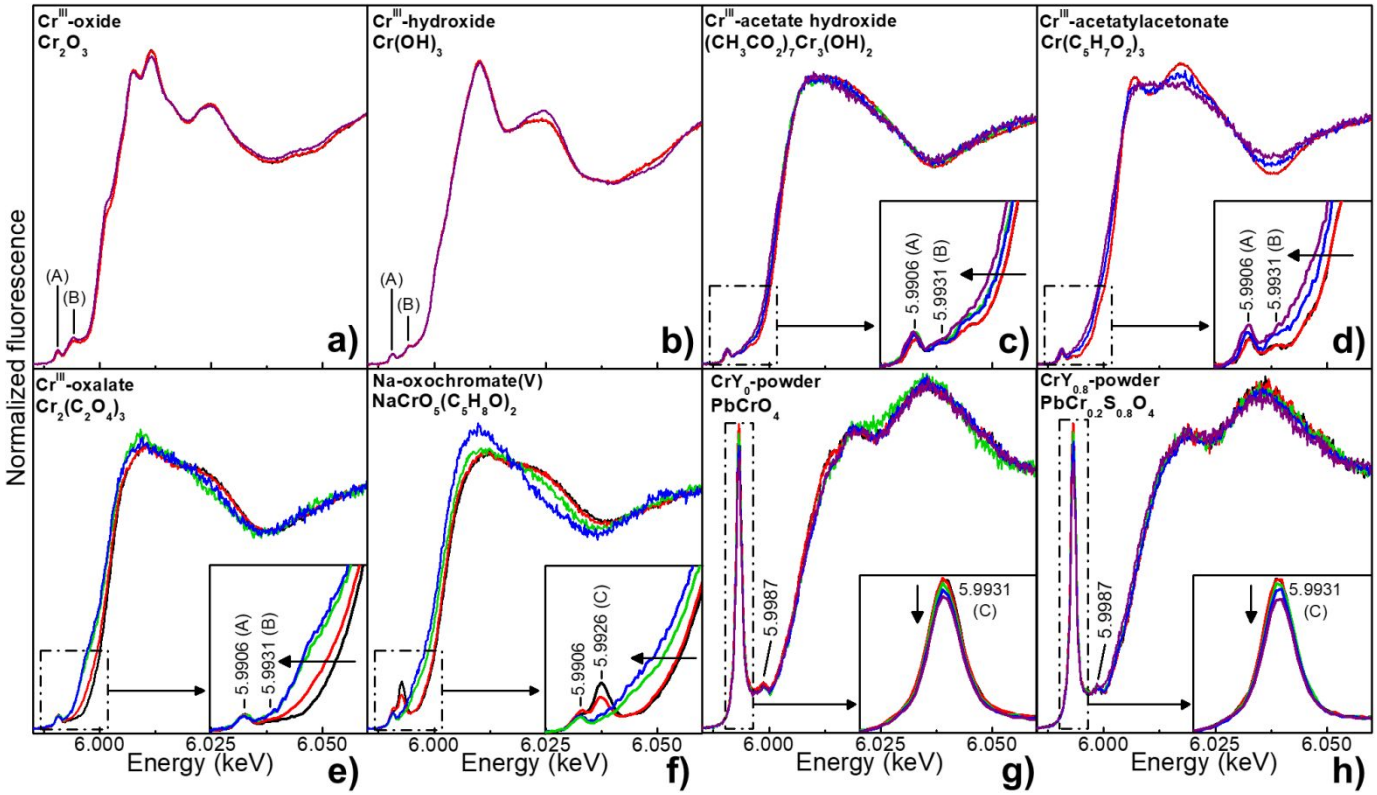

Figure 1. Cr K-edge XANES spectra of Cr-powders acquired at increasing fluences/doses at ESRF-ID21: **(a)** Cr^{III}-oxide, **(b)** Cr^{III}-hydroxide, **(c)** Cr^{III}-acetate hydroxide, **(d)** Cr^{III}-acetylacetonate, **(e)** Cr^{III}-oxalate, **(f)** Na-oxochromate(V), **(g)** CrY_0-powder, **(h)** $CrY_{0.8}$-powder [black: 1.7×10^7 ph/µm^2 (0.1-0.6 MGy); red: 1.7×10^8 ph/µm^2 (1-6 MGy); green: ~5.7×10^{11} ph/µm^2 (~5×10^3-2×10^4 MGy); blue:1-2×10^{12} ph/µm^2 (~9×10^3-4×10^4 MGy); purple: 1-2×10^{13} ph/µm^2 (~2-4×10^5 MGy)].

With the aim of obtaining complementary information to XANES, we then analyzed the Cr-powders by Cr-K_β XES. So far, this method has never been used to study the degradation of chrome yellows. Cr-K_β valence-to-core (vtc) XES can be employed to determine the chemical nature of different ligands in the first coordination shell around Cr-ions;[47,48,49,50] thus it is expected to contribute to a better understanding of the nature of various Cr^{III}-/Cr^{V}-degradation products (e.g., oxides and/or organo-Cr-complexes), which may have originated from the alteration process of chrome yellow paints.

The K_β emission spectra of Cr-powders consist of two different regions.[47-51] The first one (Figure 2: leftmost panel; Figure S3) includes the $K_{\beta1,3}$ main line and a weak band at lower energy named $K_{\beta'}$; the latter results from a core-to-core 3p→1s transition. Such lines are sensitive to the unpaired electrons in the Cr 3d orbitals, thus providing information on the Cr-oxidation state: as the oxidation state increases, the $K_{\beta1,3}$ position shifts to lower energies, while the $K_{\beta'}$ intensity decreases. The second region shows the K_β satellite lines (Figure 2: rightmost panel). These features arise from vtc transitions, involving electrons occupying valence molecular orbitals having ligand p or s type character which fills-in Cr 1s orbital, and includes the $K_{\beta2,5}$ lines and $K_{\beta''}$ or cross-over peaks. The $K_{\beta''}$ intensity and position are sensitive to the ligand (L) nature and show strong dependency on the chromium's local symmetry,[51] being more intense and shifted at higher energies in tetrahedral CrY_0 and $CrY_{0.8}$ samples than in octahedral Cr^{III}-oxides. The $K_{\beta''}$ intensity also depends on the magnitude of Cr−L orbital overlap,[48] thus providing a reasonable explanation to why such band is very weak in the organo-Cr^{III} and Cr^{V} complexes profiles. The $K_{\beta2,5}$ transitions appear as a single band in the Cr-oxides and Cr^{VI}-compounds spectra, whereas it is split into a doublet in the organo-Cr^{III}/Cr^{V} complexes profiles. Differences of the shape and position of such peaks reflect instead the different nature of the Cr-L chemical bond.

Cr-K_β XES spectra of organo-Cr^{III} and -Cr^{V} complexes recorded at "high-fluence" (~10^{10} ph/μm^2; Figure 2: red lines) show important differences with respect to the "low-fluence"

ones (~10^8 ph/μm^2; black lines). For organo-Cr^{III} compounds, while no changes are visible in the K_β main lines, a loss of structure and broadening is visible in the K_β satellite lines. In line with Cr K-edge μ-XANES results (Figure 1), such changes are attributable to modifications of the ligands' structure and/or weakening/breaking of the Cr-L bond. For the Cr^V-compound, the "high-fluence" conditions have promoted the reduction of Cr^V to Cr^{III}-species along with changes in the coordination of the Cr-ions. This is proved by the shift towards higher energies of the $K_{\beta 1,3}$ band and by modifications of the shape of K_β satellite lines. No meaningful changes are observed between the "high-fluence" and the "low-fluence" spectra of Cr_2O_3, $Cr(OH)_3$, CrY_0-powder and $CrY_{0.8}$-powder (only the formers are shown in Figure 2).

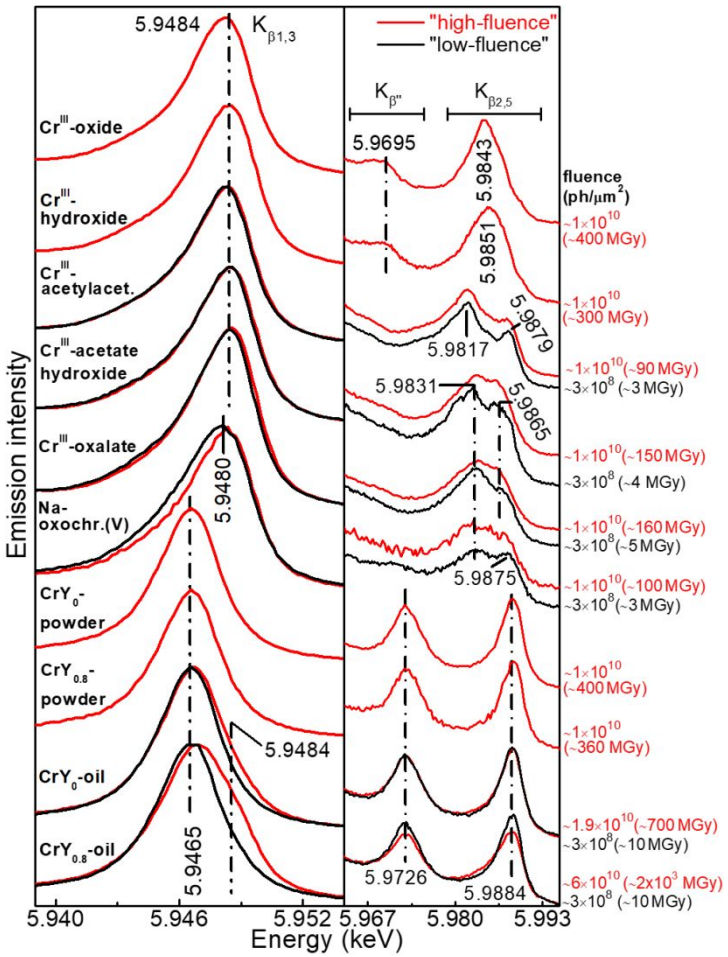

Figure 2. Cr-K_β XES spectra of Cr-samples recorded using "high-fluence" (red) and "low-fluence" (black) conditions at ESRF-ID26: (left) $K_{\beta1,3}$ line; (right) K_β satellite lines (see Figure S3 for the complete spectra of K_β main lines). Fluences along with absorbed doses (in brackets) are also reported.

3.2 Chrome yellow paints: effects of the binder and quantification of the SR X-ray-induced damage

To monitor and quantitatively evaluate the effects of SR X-rays on chrome yellows in relation to the presence and nature of the binder, we then performed a series of damage tests on paint mock-ups prepared by mixing CrY_0 or $CrY_{0.8}$-powders with either linseed oil or acrylic.

Figure 3 (black symbols) shows the plots of Cr^{III}-relative amount percentage *vs.* fluence/absorbed dose obtained *via* LCF of different Cr-references to the series of XANES spectra recorded from each chrome yellow sample at room temperature (see Figure S4 for details). The Cr^{III}-abundance exponentially increases with increasing fluence up to ~3.5×10^{13} ph/μm^2 (~1.2×10^6 MGy), achieving its highest value for $CrY_{0.8}$-oil (~35%). Under the same irradiation conditions, the reactivity of $CrY_{0.8}$-acrylic is higher than that of $CrY_{0.8}$-powder, the final Cr^{III}-amount becoming ~30% and ~10%, respectively. The tendency of CrY_0-samples to undergo reduction is lower than that of the equivalent $CrY_{0.8}$ ones. Notably, CrY_0-oil and CrY_0-acrylic reveal a similar stability under SR X-ray exposure, giving rise to the formation of Cr^{III}-abundances not greater than 20%. For CY_0-powder, the Cr^{III}-amount remains below 5%. For both chrome yellow types, the increased tendency to undergo photo-reduction in the presence of the binder can be justified considering the strong sensitivity of organic materials under SR X-ray irradiation. Organic bonds can be easily broken, thus giving rise to radicals, which can further contribute to Cr^{VI}-reduction.[5,33]

Under “high-fluence” conditions, changes in XES data are also more pronounced for $CrY_{0.8}$ and when oil is present as binder (Figure 2, CrY_0-oil and $CrY_{0.8}$-oil spectra). The $K_{\beta1,3}$ broadening, through the presence of shoulder at ~5.9484 keV, and variations in the relative intensity of K_β satellite lines are attributable to the formation of Cr^{III}-compounds and modifications of Cr-ions coordination.

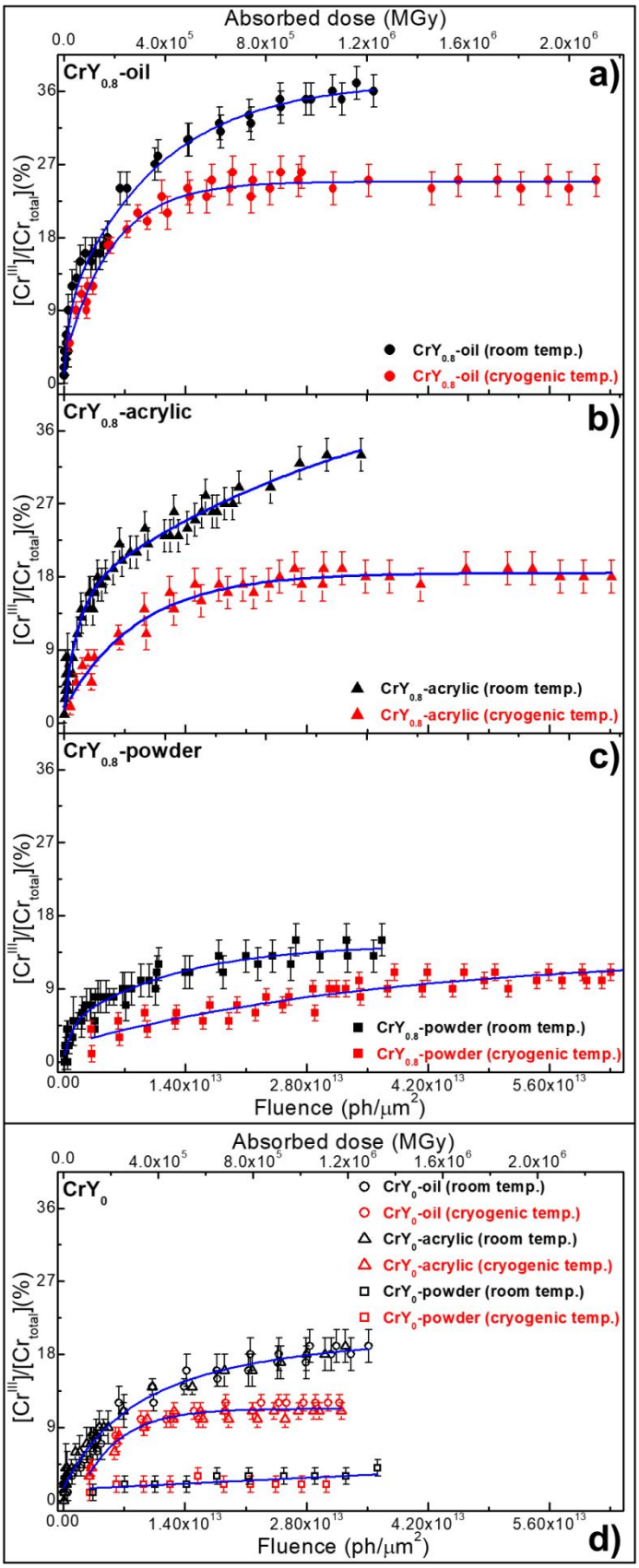

Figure 3. Plots of Cr^{III}-relative amount percentage *vs.* fluence/absorbed dose obtained at room temperature (black) and cryogenic temperature (red) at ESRF-ID21: **(a-c)** $CrY_{0.8}$-samples; **(d)** CrY_0-samples. In blue, fit obtained using mono-exponential or bi-exponential functions.

Chemical changes induced by "high-fluence" XES occur along with a "burning" of the paint surface (Figure 4a,b). Such phenomenon is not apparent in the same samples analyzed at "low-fluence". Cr K-edge μ-XANES analysis of "burnt" areas permitted to monitor and quantitatively evaluate the extent of damage (Figure 4c,d). As expected, before XES, the μ-XANES spectra resemble to the ones typically obtained for chrome yellows;[24] after XES, Cr-oxidation state maps combined with μ-XANES measurements show that the "burnt" areas contain higher Cr^{III}-amounts in $CrY_{0.8}$-oil (~35%) than in CrY_0-oil (~13%). Vibrational micro-spectroscopies revealed that the alteration of the binder has also occurred in addition to that of the pigment (Figure S5).

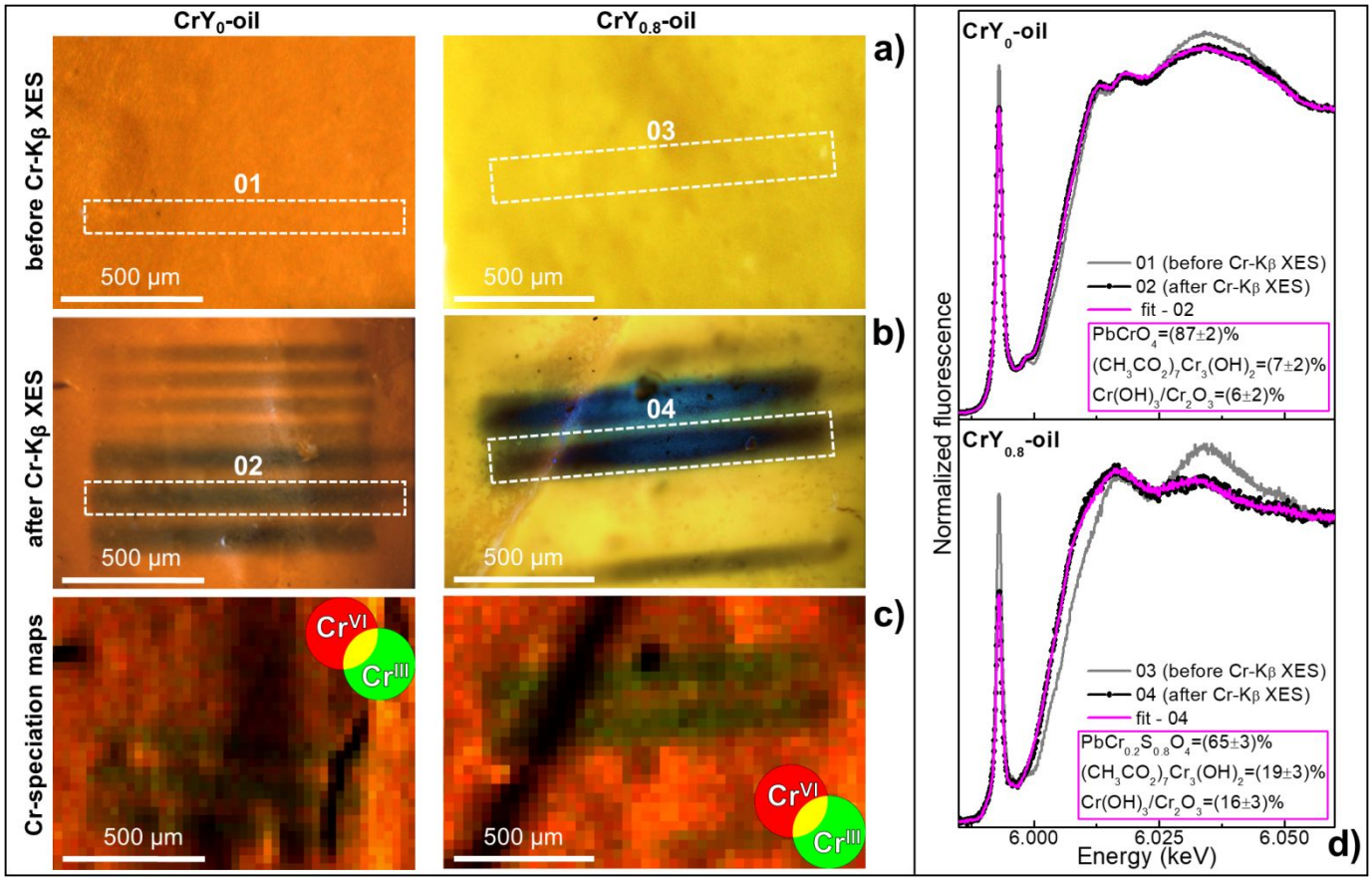

Figure 4. Photomicrographs of CrY_0-oil and $CrY_{0.8}$-oil **(a)** before and **(b)** after "high-fluence" Cr-K_β XES investigations (*cf.* Figure 2 for the corresponding XES spectra). **(c)** RG composite SR μ-XRF Cr^{VI}/Cr^{III} maps recorded from the areas shown in (b) at ESRF-ID21 [step size (h×v): 30×30 μm^2; exp. time: 100 ms/pixel]. **(d)** Cr K-edge XANES spectra (grey and black) recorded at ESRF-ID26 from the regions shown by the rectangles in (a,b) and corresponding LCF results (magenta).

In Figure 5a,b, XRD patterns obtained at increasing fluences/doses are shown for CrY_0-/ $CrY_{0.8}$-oil paints. As reported earlier,[34] CrY_0 contains only monoclinic $PbCrO_4$ (Figure 5a: green bars), while monoclinic $PbCr_{0.4}S_{0.6}O_4$ and orthorhombic $PbCr_{0.1}S_{0.9}O_4$ are present in $CrY_{0.8}$ (Figure 5b: black and red bars). In order to compare samples, the intensity decay profiles for the crystalline compounds have been normalized to their initial total integrated diffraction peak intensity (i.e. at the lowest fluence value). For both monoclinic structures, the total intensity of their diffraction peaks decreases with increasing fluence/dose (Figure 5c,d), indicating a loss in crystallinity. For a fluence of 7.5×10^{12} ph/μm^2 (~1.5×10^5 MGy), the $PbCr_{0.4}S_{0.6}O_4$ diffraction intensity decreases to ~10-20% in all $CrY_{0.8}$-samples, while that of $PbCrO_4$ is diminished to 40-50% in the CrY_0-samples at the same fluence. A decay in diffraction intensity induced by intense SR X-ray beams is well-known in the field of biocrystallography and is caused by a sequential process: first there is an increase in disorder within the crystal structure after which the structure is rendered amorphous.[52,53] Indeed, the conversion of the crystalline monoclinic phases into a poorly structured/amorphous material with increasing fluences/doses is suggested by the formation of a broad band (at Q=19.5 nm^{-1}). The intensity of this band has been normalized to the last intensity (i.e. at the highest fluence value). For CrY_0-samples (Figure 5a, inset and Figure 5e), its formation occurs starting from ~2-4$\times10^{11}$ ph/μm^2 (~4-8$\times10^3$ MGy) and its intensity gradually increases up to ~1.5×10^{13} ph/μm^2 (~2.5×10^5 MGy). For $CrY_{0.8}$-samples, such signal can hardly be seen due to the low abundance of $PbCr_{0.4}S_{0.6}O_4$.[34]

While the monoclinic phases show a strong X-ray sensitivity, the total integrated diffraction peak intensity of orthorhombic $PbCr_{0.1}S_{0.9}O_4$ (the most abundant compound in $CrY_{0.8}$) stays fairly unchanged over the entire fluence range. Its intensity drops slightly to ~80% at 7.5×10^{12} ph/μm^2 (~1.5×10^5 MGy) and does not change further up to 2.5×10^{13} ph/μm^2 (~4×10^5 MGy) (Figure 5f).

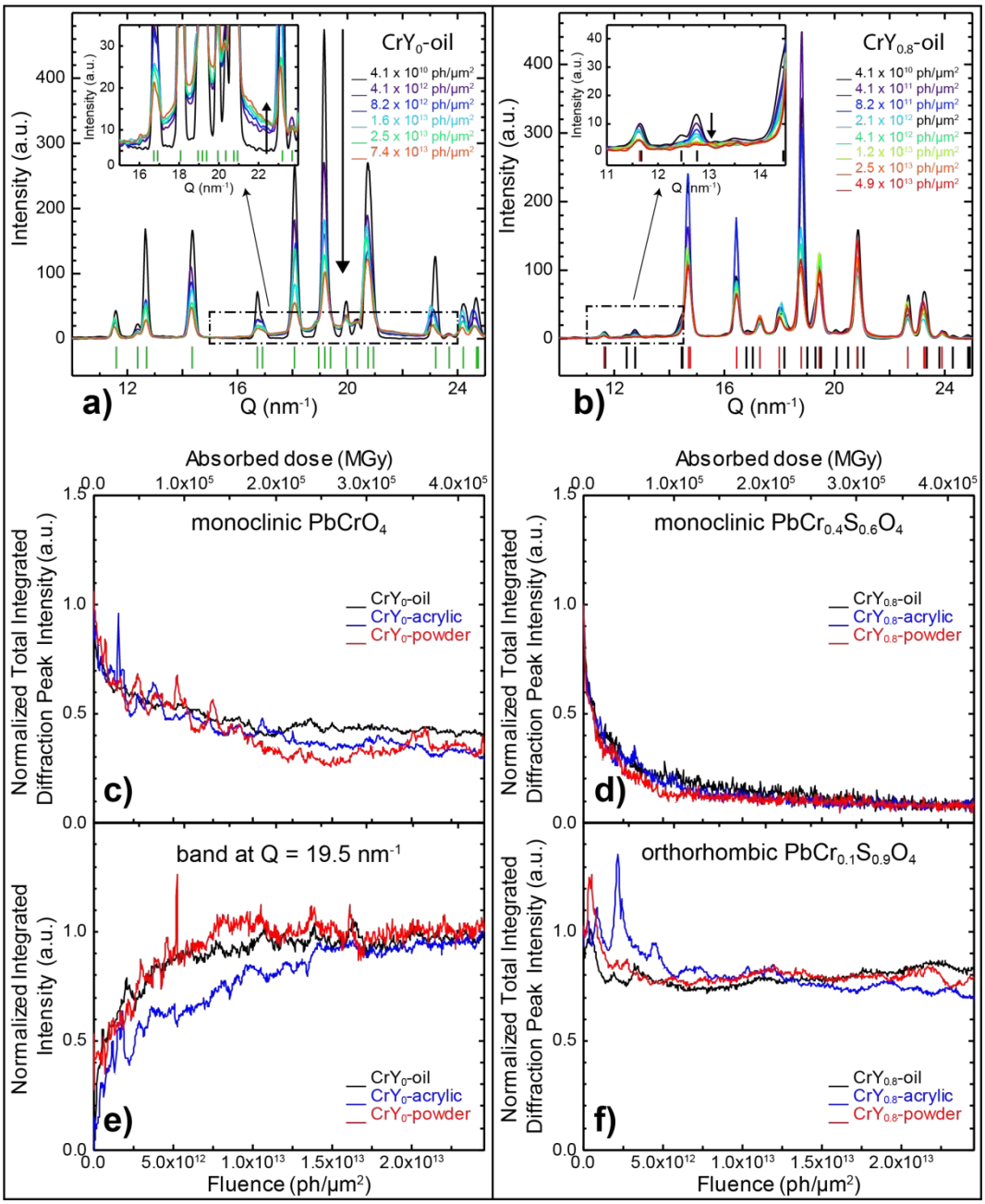

Figure 5. µ-XRD patterns collected from **(a)** CrY_0-oil and **(b)** $CrY_{0.8}$-oil at increasing fluences/doses at DESY-P06. Vertical bars indicate the diffraction peak positions of monoclinic $PbCrO_4$ (green), monoclinic $PbCr_{0.4}S_{0.6}O_4$ (black) and orthorhombic $PbCr_{0.1}S_{0.9}O_4$ (red). Normalized integrated intensity *vs.* fluence/absorbed dose of **(c)** monoclinic $PbCrO_4$, **(d)** monoclinic $PbCr_{0.4}S_{0.6}O_4$, **(e)** amorphous phase and **(f)** orthorhombic $PbCr_{0.1}S_{0.9}O_4$ in CrY_0-/$CrY_{0.8}$-samples (black=oil; blue=acrylic; red=powder).

The "burnt" areas caused by µ-XRD in CrY-oil paints were further investigated by Cr-speciation analysis, revealing that the X-ray exposure has also led to the formation of Cr^{III}-compounds (Figure S6).

3.3. Mitigation strategies for SR X-ray-induced damage in chrome yellows

3.3.1 Optimization of the fluence/dose. Before starting a SR X-ray analysis on a sample that is potentially sensitive to X-rays, the fluence/dose threshold at which X-rays start to induce spectral changes in the data should be assessed. At ESRF-ID21 and ESRF-ID26 (Figures 1-3; X-ray energy: ~6 keV) such values are about 5×10^{11} ph/μm^2 (~2×10^4 MGy) and 10^8 ph/μm^2 (~10 MGy), respectively, and the significant difference between the two is mainly due to the use of vacuum at ESRF-ID21. At DESY-P06 (Figure 5; X-ray energy: 21 keV, no vacuum) this is ~1-2×10^{11} ph/μm^2 (~2-4×10^3 MGy).

Once the threshold fluence/dose under specific conditions has been determined, the data acquisition time should be adapted to stay below this threshold value when possible (Figures 1-3,5). If fast-data acquisition is not feasible, an alternative is to decrease the flux of the incoming beam (e.g., using attenuators of different thickness; see Figure S7) as long as an adequate signal-to-noise-ratio is maintained. When the fluence/dose limit is reached and the statistics are not satisfactory, one can analyse several spots on the sample and average their response. However, this is feasible only when spatial resolution is not an issue and if samples are sufficiently large (order of tenths of mm^2) and compositionally homogenous (Figure 2, “low-fluence” data). Defocusing the beam is another strategy to minimize the fluence/dose to the sample, but sometimes at the expense of spectral resolution (e.g. XES analysis).

3.3.2. Measuring under vacuum conditions. For similar doses, the photo-induced reduction is less pronounced for samples analyzed at ESRF-ID21, with respect to those investigated at ESRF-ID26 and DESY-P06. For example, in the case of $CY_{0.8}$-oil, measurements performed at room temperature using ~2×10^3 MGy at ESRF-ID21 and ESRF-ID26 led to the production of Cr^{III}-abundances smaller than 5% and of ~35%, respectively (Figures 3a,4d). In the same sample, experiments carried out using ~8×10^5 MGy at ESRF-ID21 and DESY-P06 induced the formation of Cr^{III}-amounts of ~35% and

~45%, respectively (Figure 3a, Figure S6). The lower Cr^{III}-abundances obtained at ESRF-ID21 can be explained considering that these measurements were conducted under vacuum conditions. According to literature,[5] such sample environment may contribute to indirectly slowing down Cr-reduction due to the absence/neglectable content of air gases (e.g. O_2) and moisture, which favor the oxidative degradation of the binder.

3.3.3. Lowering the temperature. Cryo-preservation is routinely used for the study of biological systems.[53,54] Cooling results in a reduction of diffusive processes and hinders the extensive propagation of ions and radicals.[5,55] Such strategy is rarely considered for the analysis of artistic materials. Thus, we decided to assess its efficiency for chrome yellows.

Figure 3 shows the comparison between the plots of Cr^{III}- percentage abundance *vs.* fluence/absorbed dose recorded from chrome yellow samples at room temperature (black symbols) and under cryogenic conditions (red symbols). At low temperature, the (smaller) reactivity of CrY_0-powder remains the same under SR X-ray irradiation (Figure 3d), while the photo-induced Cr^{VI}-reduction slows down for all the other samples. Compared to the room temperature measurements, the final Cr^{III}-amount is decreased to ~40-45% for $CrY_{0.8}$-acrylic, CrY_0-oil and CrY_0-acrylic (Figure 3b,d), and it is diminished at ~30% for $CrY_{0.8}$-oil and $CrY_{0.8}$-powder (Figure 3a,c). Thus, similarly to what was already observed for other Cr-based materials in different contexts,[46,56] recording spectra at cryogenic temperature contributes to mitigate the SR X-ray-induced damage of chrome yellows.

In addition, in CrY_0/ $CrY_{0.8}$-oil and -acrylic mock-ups, the increasing of Cr^{III}-abundance *vs.* fluence is well described by a bi-exponential function (R^2>0.98) for room temperature experiments , while it is adequately fitted by a mono-exponential function (R^2>0.93) for those performed under cryogenic conditions and for the CrY_0/$CrY_{0.8}$-powders (see the fits as blue lines in Fig. 3). Such results suggest that at room temperature, a second Cr-reduction pathway, developing in the presence of reactive species arising from the binder degradation (e.g. radicals), becomes activated at higher fluences.

4. Conclusions

In this work, a combination of SR-based X-ray techniques, namely Cr K-edge XANES, Cr-K_β XES and μ-XRD, allowed us to monitor and quantify the X-ray-induced damage in chrome yellows and related Cr-compounds and to define strategies to mitigate such damage. Our results proved that SR X-rays induce changes in the oxidation state and local coordination environment of Cr-ions and promote changes of the compound's crystalline structure.

Under equivalent irradiation conditions, the extent of damage depends on the nature of the analyzed sample. Organo-Cr^{III}-complexes are more prone to change than Cr^{III}-oxides. For chrome yellows ($PbCrO_4$ and $PbCr_{0.2}S_{0.8}O_4$), modifications are more pronounced for the $PbCr_{0.2}S_{0.8}O_4$ type and when the pigment is mixed with a binder. This result shows how crucial it is to evaluate X-ray sensitivity on systems as similar as possible to the real paints, rather than on pure powders. Studies on SR X-ray-induced effects on the binder in chrome yellow paints are still ongoing, and their results will be published in follow-up papers.

A first strategy to minimize the X-ray-induced damage of chrome yellows is to employ fluences not greater than 10^{10}-10^{11} ph/μm^2. The use of larger solid angle detectors,[27,57] may contribute to further reduce the overall dose released to samples. Two other strategies consist in working in vacuum and under cryogenic conditions. Cryo-preservation is expected to be more regularly employed for future analysis of X-ray sensitive mock-ups and historical painting fragments. However, a long-term monitoring of samples will be required to assess the occurrence of any delayed damages due to temperature changes. Related to that, where feasible, the preparation of paint thin-sections by a microtome should be considered, so as to keep the rest of the cross-section available for other experiments.

If the X-ray-induced damage cannot be fully prevented, it is important to: i) quantitatively assess its contribution to the signal; ii) analyze all samples with the same exposure conditions; iii) well-document the damage to prevent erroneous future analyses. Generally,

care should be taken when comparing data obtained using different X-ray beams and sample conditioning during analysis at various beamlines.

Overall, our findings contribute to define a safe analytical protocol for chrome yellows investigations by SR X-ray methods, which allows for avoiding misinterpretations of data finalized to the study of their degradation mechanism and to prevent damage of historical samples.

Associated Content

Supporting Information

The Supporting Information is available free of charge at xxxx

Cr-oxidation state mapping and LCF of Cr K-edge XANES spectra; calculation of the absorbed dose; determination of photon flux at ESRF-ID26; additional XES/XANES and vibrational micro-spectroscopy data on chrome yellow samples; Relationship between the X-ray photo-induced Cr^{III}-reduction and fluence rate.

Acknowledgments

The research was financially supported by: the EU projects IPERION-CH (grant agreement no. 654028, H2020-INFRAIA-2014-2015) and CALIPSOplus (grant agreement no. 730872, H2020-EU.1.4.1.2.); the project AMIS (Dipartimenti di Eccellenza 2018-2022, funded by MIUR and Perugia University). For the beamtime grants received, we thank: ESRF-ID21/ID26 (experiment nos. HG64, HG129, HG98; in-house beamtimes). Portions of this research was performed at Petra-III, P06 at DESY, a member of the Helmholtz Association (HGF) (experiment nos. I-20160672 EC, I-20170721 EC). L.M. acknowledges the Erasmus+ Programme (Staff Mobility for training, 2018-2019). K.J., F.V. and G.N. acknowledge the Research Council of the University of Antwerp for support via BOF GOA Project Solarpaint and Interreg Project Smart*Light.

References

[1] Bertrand, L.; Bernard, S.; Marone, F.; Thoury, M.; Reiche, I.; Gourrier, A.; Sciau, P.; Bergmann U. Emerging approaches in synchrotron studies of materials from cultural and natural history collections. *Top. Curr. Chem.* **2016**, *374*, 1-39.

[2] Cotte, M.; Genty-Vincent, A.; Janssens, K.; Susini, J. Applications of synchrotron X-ray nano-probes in the field of cultural heritage. *C. R. Phys.* **2018**, *19*, 575-588.

[3] Janssens, K.; Van der Snickt, G.; Vanmeert, F.; Legrand, S.; Nuyts, G.; Alfeld, M.; Monico, L.; Anaf, W.; De Nolf, W.; Vermeulen, M.; Verbeeck, J.; De Wael, K. Non-invasive and non-destructive examination of artistic pigments, paints, and paintings by means of X-ray methods. *Top. Curr. Chem.* **2016**, *374*, 77-128.

[4] Gonzalez, V.; Cotte, M.; Vanmeert, F.; De Nolf, W.; Janssens, K. X-ray diffraction mapping for cultural heritage science: a review of experimental configurations and applications. *Chem.-Eur. J.* **2020**, *26,* 1703-1719.

[5] Bertrand, L.; Schöeder, S.; Anglos, D.; Breese, M.B.; Janssens, K.; Moini, M.; Simon, A. Mitigation strategies for radiation damage in the analysis of ancient materials. *TrAC, Trends Anal. Chem.* **2015**, *66,* 128-145.

[6] Gervais, C.; Languille, M.A.; Reguer, S.; Gillet, M.; Vicenzi, E.P.; Chagnot, S.; Baudelet, F.; Bertrand, L. “Live” Prussian blue fading by time-resolved X-ray absorption spectroscopy. *Appl. Phys. A: Mater. Sci. Process.* **2013**, *111*, 15-22.

[7] Gervais, C.; Languille, M.A.; Moretti, G.; Réguer, S. X-ray photochemistry of prussian blue cellulosic materials: evidence for a substrate-mediated redox process. *Langmuir* **2015**, *31,* 8168-8175.

[8] Gervais, C.; Thoury, M.; Réguer, S.; Gueriau, P.; Mass, J. Radiation damages during synchrotron X-ray micro-analyses of Prussian blue and zinc white historic paintings: detection, mitigation and integration. *Appl. Phys. A: Mater. Sci. Process.* **2015**, *121*, 949-955.

[9] Ganio, M.; Pouyet, E. S.; Webb, S. M.; Patterson, C.M.S.; Walton, M.S. From lapis lazuli to ultramarine blue: investigating Cennino Cennini's recipe using sulfur K-edge XANES. *Pure Appl. Chem.* **2018***, 90,* 463-475.

[10] Cato, E.; Borca, C.; Huthwelker, T.; Ferreira, E.S. Aluminium X-ray absorption near-edge spectroscopy analysis of discoloured ultramarine blue in 20th century oil paintings. *Microchem. J.* **2016**, *126,* 18-24.

[11] Radepont, M.; De Nolf, W.; Janssens, K.; Van der Snickt, G.; Coquinot, Y.; Klaassen, L.; Cotte, M. The use of microscopic X-ray diffraction for the study of HgS and its degradation products corderoite (α-Hg_3S2Cl_2), kenhsuite (γ-$Hg_3S_2Cl_2$) and calomel (Hg_2Cl_2) in historical paintings. *J. Anal. At. Spectrom.* **2011**, *26,* 959-968.

[12] Vanmeert, F.; Van der Snickt, G.; Janssens, K. Plumbonacrite identified by X-ray powder diffraction tomography as a missing link during degradation of red lead in a Van Gogh painting. *Angew. Chem., Int. Ed.* **2015**, *54,* 3607-3610.

[13] Mass, J.L.; Opila, R.; Buckley, B.; Cotte, M.; Church, J.; Mehta, A. The photodegradation of cadmium yellow paints in Henri Matisse's *Le Bonheur de vivre* (1905–1906). *Appl. Phys. A: Mater. Sci. Process.* **2013**, *111*, 59-68.

[14] Pouyet, E.; Cotte, M.; Fayard, B.; Salomé, M.; Meirer, F.; Mehta, A.; Uffelman, E.S.; Hull, A.; Vanmeert, F.; Kieffer, J.; Burghammer, M.; Janssens, K.; Sette, F.; Mass, J. 2D X-ray and FTIR micro-analysis of the degradation of cadmium yellow pigment in paintings of Henri Matisse. *Appl. Phys. A: Mater. Sci. Process.* **2015**, *121*, 967-980.

[15] Van der Snick, G.; Dik, J.; Cotte, M.; Janssens, K.; Jaroszewicz, J.; De Nolf, W.; Groenewegen, J.; Van der Loeff, L. Characterization of a degraded cadmium yellow (CdS) pigment in an oil painting by means of synchrotron radiation based X-ray techniques. *Anal. Chem.* **2009***, 81,* 2600-2610.

[16] Van der Snickt, G.; Janssens, K.; Dik, J.; De Nolf, W.; Vanmeert, F.; Jaroszewicz, J.; Cotte, M.; Falkenberg, G.; Van der Loeff, L. Combined use of Synchrotron Radiation Based Micro-X-ray Fluorescence, Micro-X-ray Diffraction, Micro-X-ray Absorption Near-Edge, and Micro-Fourier Transform Infrared Spectroscopies for Revealing an Alternative Degradation Pathway of the Pigment Cadmium Yellow in a Painting by Van Gogh. *Anal. Chem.* **2012**, *84,* 10221-10228.

[17] Monico, L.; Chieli, A.; De Meyer, S.; Cotte, M.; De Nolf, W.; Falkenberg, G.; Janssens, K.; Romani, A.; Miliani, C. Role of the Relative Humidity and the Cd/Zn Stoichiometry in the Photooxidation Process of Cadmium Yellows (CdS/$Cd_{1-x}Zn_xS$) in Oil Paintings. *Chem.-Eur. J.* **2018**, *24*, 11584-11593.

[18] Monico, L.; Cartechini, L.; Rosi, F.; Chieli, A.; Grazia, C.; De Meyer, S.; Nuyts, G.; Vanmeert, F.; Janssens, K.; Cotte, M.; De Nolf, W.; Falkenberg, G.; Crina Anca Sandu, I.; Storevik Tveit, E.; Mass, J.; Pereira de Freitas, R.; Romani, A.; Miliani, C. Probing the chemistry of CdS paints in *The Scream* by in situ noninvasive spectroscopies and

synchrotron radiation x-ray techniques *Sci. Adv.* **2020**, *6*, eaay3514, doi: 10.1126/sciadv.aay3514.

[19] Keune, K.; Mass, J.; Meirer, F.; Pottasch, C.; van Loon, A.; Hull, A.; Church, J.; Pouyet, E.; Cotte, M.; Mehta, A. Tracking the transformation and transport of arsenic sulfide pigments in paints: synchrotron-based X-ray micro-analyses. *J. Anal. At. Spectrom.* **2015**, *30,* 813-827.

[20] Vermeulen, M.; Nuyts, G.; Sanyova, J.; Vila, A.; Buti, D.; Suuronen, J. P.; Janssens, K. Visualization of As (III) and As (V) distributions in degraded paint micro-samples from Baroque-and Rococo-era paintings. *J. Anal. At. Spectrom.* **2016***, 31,* 1913-1921.

[21] Keune, K.; Mass, J.; Mehta, A.; Church, J.; Meirer, F. Analytical imaging studies of the migration of degraded orpiment, realgar, and emerald green pigments in historic paintings and related conservation issues. *Heritage Sci.* **2016**, *4*, 10, doi: 10.1186/s40494-016-0078-1.

[22] Simoen, J.; De Meyer, S.; Vanmeert, F.; de Keyser, N.; Avranovich, E.; Van der Snickt, G.; Van Loon, A.; Keune, K.; Janssens, K. Combined Micro-and Macro scale X-ray powder diffraction mapping of degraded Orpiment paint in a 17th century still life painting by Martinus Nellius. *Heritage Sci.* **2019***, 7,* 83, doi: 10.1186/s40494-019-0324-4.

[23] Zanella, L.; Casadio, F.; Gray, K.A.; Warta, R.; Mac, Q.; Gaillard, J.F. The darkening of zinc yellow: XANES speciation of chromium in artist's paints after light and chemical exposures. *J. Anal. At. Spectrom.* **2011**, *26,* 1090-1097.

[24] Monico, L.; Van der Snickt, G.; Janssens, K.; De Nolf, W.; Miliani, C.; Verbeeck, J.; Tian, H.; Tan, H.; Dik, J.; Radepont, M.; Cotte, M. Degradation Process of Lead Chromate in Paintings by Vincent van Gogh Studied by Means of Synchrotron X-ray Spectromicroscopy and Related Methods. 1. Artificially Aged Model Samples. *Anal. Chem.* **2011***, 83*, 1214-1223.

[25] Monico, L.; Van der Snickt, G.; Janssens, K.; De Nolf, W.; Miliani, C.; Dik, J.; Radepont, M.; Hendriks, E.; Geldof, M.; Cotte, M. Degradation Process of Lead Chromate in Paintings by Vincent van Gogh Studied by Means of Synchrotron X-ray Spectromicroscopy and Related Methods. 2. Original Paint Layer Samples. *Anal. Chem.* **2011***, 83,* 1224-1231.

[26] Monico, L.; Janssens, K.; Vanmeert, F.; Cotte, M.; Brunetti, B.G.; Van der Snickt, G.; Leeuwestein, M.; Salvant Plisson, J.; Menu, M.; Miliani, C. Degradation Process of Lead Chromate in Paintings by Vincent van Gogh Studied by Means of Spectromicroscopic

Methods. Part 5. Effects of Nonoriginal Surface Coatings into the Nature and Distribution of Chromium and Sulfur Species in Chrome Yellow Paints. *Anal. Chem.* **2014***, 86,* 10804-10811.

[27] Monico, L.; Janssens, K.; Alfeld, M.; Cotte, M.; Vanmeert, F.; Ryan, C.G.; Falkenberg, G.; Howard, D.L.; Brunetti, B.G.; Miliani, C. Full spectral XANES imaging using the Maia detector array as a new tool for the study of the alteration process of chrome yellow pigments in paintings by Vincent van Gogh. *J. Anal. At. Spectrom.* **2015***, 30,* 613-626.

[28] Monico, L.; Janssens, K.; Hendriks, E.; Vanmeert, F.; Van der Snickt, G.; Cotte, M.; Falkenberg, G.; Brunetti, B.G.; Miliani, C. Evidence for Degradation of the Chrome Yellows in Van Gogh's Sunflowers: A Study Using Noninvasive In-Situ Methods and Synchrotron-Radiation-Based X-ray Techniques. *Angew. Chem., Int. Ed.* **2015***, 54,* 13923-13927.

[29] Monico, L.; Janssens, K.; Miliani, C.; Van der Snickt, G.; Brunetti, B.G.; Cestelli Guidi, M.; Radepont, M.; Cotte, M. Degradation Process of Lead Chromate in Paintings by Vincent van Gogh Studied by Means of Spectromicroscopic Methods. 4. Artificial Aging of Model Samples of Co-Precipitates of Lead Chromate and Lead Sulfate. *Anal. Chem.* **2013**, *85,* 860-867.

[30] Otero, V.; Vilarigues, M.; Carlyle, L.; Cotte, M.; De Nolf, W.; Melo, M.J. A little key to oxalate formation in oil paints: protective patina or chemical reactor? *Photochem. Photobiol. Sci.* **2018***, 17,* 266-270.

[31] Monico, L.; Janssens, K.; Cotte, M.; Romani, A.; Sorace, L.; Grazia, C.; Brunetti, B.G.; Miliani, C. Synchrotron-based X-ray spectromicroscopy and electron paramagnetic resonance spectroscopy to investigate the redox properties of lead chromate pigments under the effect of visible light. *J. Anal. At. Spectrom.* **2015***, 30,* 1500-1510.

[32] Monico, L.; Janssens, K.; Cotte, M.; Sorace, L.; Vanmeert, F.; Brunetti, B.G.; Miliani, C. Chromium speciation methods and infrared spectroscopy for studying the chemical reactivity of lead chromate-based pigments in oil medium. *Microchem. J.* **2016**, *124*, 272-282.

[33] Monico, L.; Sorace, L.; Cotte, M.; De Nolf, W.; Janssens, K.; Romani, A.; Miliani, C. Disclosing the Binding Medium Effects and the Pigment Solubility in the (Photo)reduction Process of Chrome Yellows ($PbCrO_4$/$PbCr_{1-x}S_xO_4$). *ACS Omega* **2019***, 4,* 6607-6619.

[34] Monico, L.; Janssens, K.; Miliani, C.; Brunetti, B.G.; Vagnini, M.; Vanmeert, F.; Falkenberg, G.; Abakumov, A.; Lu, Y.; Tian, H.; Verbeeck, J.; Radepont, M.; Cotte, M.;

Hendriks, E.; Geldof, M.; van der Loeff, L.; Salvant, J.; Menu, M. Degradation Process of Lead Chromate in Paintings by Vincent van Gogh Studied by Means of Spectromicroscopic Methods. 3. Synthesis, Characterization, and Detection of Different Crystal Forms of the Chrome Yellow Pigment. *Anal. Chem.* **2013***, 85,* 851-859.

[35] Roy, A. Monet's Palette in the Twentieth Century: Water-Lilies and Irises. *National Gallery Technical Bulletin* **2007**, *28,* 58-68.

[36] Cotte, M.; Pouyet, E.; Salome, M.; Rivard, C.; De Nolf, W.; Castillo-Michel, H.; Fabris, T.; Monico, L.; Janssens, K.; Wang, T.; Sciau, P.; Verger, L.; Cormier, L.; Dargaud, O.; Brun, E.; Bugnazet, D.; Fayard, B.; Hesse, B.; Pradas del Real, A.; Veronesi, G.; Langlois, J.; Balcar, N.; Vandenberghe, Y.; Sole, V.A.; Kieffer, J.; Barrett, R.; Cohen, C.; Cornu, C.; Baker, R.; Gagliardini, E.; Papillon, E.; Susini, J. The ID21 X-ray and infrared microscopy beamline at the ESRF: status and recent applications to artistic materials. *J. Anal. At. Spectrom.* **2017***, 32,* 477-493.

[37] Cotte, M.; Fabris, T.; Agostini, G.; Motta Meira, D.; De Viguerie, L.; Solé, V.A. Watching kinetic studies as chemical maps using open-source software. *Anal. Chem.* **2016***, 88,* 6154-6160.

[38] Salomé, M.; Cotte, M.; Baker, R.; Barrett, R.; Benseny-Cases, N.; Berruyer, G.; Bugnazet, D.; Castillo-Michel, H.; Cornu, C.; Fayard, B.; Gagliardini, E.; Hino, R.; Morse, J.; Papillon, E.; Pouyet, E.; Rivard, C.; Solé, V.A.; Susini, J.; Veronesi, G. The ID21 Scanning X-ray Microscope at ESRF. *J. Phys.: Conf. Ser.* **2013***, 425,* 182004.

[39] Ravel, B.; Newville, M. ATHENA, ARTEMIS, HEPHAESTUS: data analysis for X-ray absorption spectroscopy using IFEFFIT. *J. Synchrotron Radiat.* **2005**, *12*, 537-541.

[40] Schroer, C.G.; Boye, P.; Feldkamp, J.M.; Patommel, J.; Samberg, D.; Schropp, A.; Schwab, A.; Stephan, S.; Falkenberg, G.; Wellenreuther, G.; Reimers, N. Hard X-ray nanoprobe at beamline P06 at PETRA III. *Nucl. Instrum. Methods Phys. Res., Sect. A* **2010**, *616*, 93-97.

[41] De Nolf, W.; Vanmeert, F.; Janssens, K. XRDUA: crystalline phase distribution maps by two-dimensional scanning and tomographic (micro) X-ray powder diffraction. *J. Appl. Crystallogr.* **2014**, *47,* 1107–1117.

[42] Pantelouris, A.; Modrow, H.; Pantelouris, M.; Hormes, J.; Reinen, D. The influence of coordination geometry and valency on the K-edge absorption near edge spectra of selected chromium compounds. *Chem. Phys.* **2004**, *300*, 13-22.

[43] Tromp, M.; Moulin, J.; Reid, G.; Evans, J. Cr K-Edge XANES Spectroscopy: Ligand and Oxidation State Dependence—What is Oxidation State? *AIP Conf. Proc.* **2007**, *882*, 699-701.

[44] Peterson, M.L.; Jr Brown, G.E.; Parks, G.A.; Stein, C.L. Differential redox and sorption of Cr (III/VI) on natural silicate and oxide minerals: EXAFS and XANES results. *Geochim. Cosmochim. Acta* **1997***, 61,* 3399-3412.

[45] Farges, F. Chromium speciation in oxide-type compounds: application to minerals, gems, aqueous solutions and silicate glasses. *Phys. Chem. Miner.* **2009**, *36,* 463-481.

[46] Levina, A.; Codd, R.; Foran, G.J.; Hambley, T.W.; Maschmeyer, T.; Masters, A.F.; Lay, P.A. X-ray Absorption Spectroscopic Studies of Chromium (V/IV/III)−2-Ethyl-2-hydroxybutanoato (2−/1−) Complexes. *Inorg. Chem.* **2004**, *43,* 1046-1055.

[47] Eeckhout, S.G.; Safonova, O.V.; Smolentsev, G.; Biasioli, M.; Safonov, V.A.; Vykhodtseva, L.N.; Sikora, M.; Glatzel, P. Cr local environment by valence-to-core X-ray emission spectroscopy. *J. Anal. At. Spectrom.* **2009**, *24*, 215-223.

[48] MacMillan, S.N.; Walroth, R. C.; Perry, D.M.; Morsing, T.J.; Lancaster, K.M. Ligand-sensitive but not ligand-diagnostic: evaluating Cr valence-to-core X-ray emission spectroscopy as a probe of inner-sphere coordination. *Inorg. Chem.* **2015**, *54,* 205-214.

[49] Safonov, V.A.; Vykhodtseva, L.N.; Polukarov, Y.M.; Safonova, O.V.; Smolentsev, G.; Sikora, M.; Eeckhout, S.G.; Glatzel, P. Valence-to-Core X-ray Emission Spectroscopy Identification of Carbide Compounds in Nanocrystalline Cr Coatings Deposited from Cr(III) Electrolytes Containing Organic Substances. *J. Phys. Chem. B* **2006**, *110,* 23192-23196.

[50] Torres Deluigi, M.; de Groot, F.M.F.; López-Díaz, G.; Tirao, G.; Stutz, G.; Riveros de la Vega, J. Core and Valence Structures in Kβ X-ray Emission Spectra of Chromium Materials. *J. Phys. Chem. C* **2014**, *118*, 22202-22210.

[51] Gallo, E.; Glatzel, P. Valence to core X-ray emission spectroscopy. *Adv. Mater.* **2014**, *26*, 7730-7746.

[52] Nave, C. Radiation-damage in protein crystallography. *Rad. Phys. Chem.* **1995**, *45*, 483-490.

[53] Meents, A.; Gutmann, S.; Wagner, A.; Schulze-Briese, C. Origin and temperature dependence of radiation damage in biological samples at cryogenic temperatures. *Proc. Natl. Acad. Sci. U.S.A.* **2010**, *107*, 1094-1099.

[54] Castillo-Michel, H.A.; Larue, C.; del Real, A.E.P.; Cotte, M.; Sarret, G. Practical review on the use of synchrotron based micro- and nano- X-ray fluorescence mapping and X-ray absorption spectroscopy to investigate the interactions between plants and engineered nanomaterials. *Plant Physiol. Biochem.* **2017**, *110*, 13-32.

[55] Holton, J.M. A beginner's guide to radiation damage. *J. Synchrotron Radiat.* **2009,** *16,* 133–142.

[56] Weng, T.C.; van der Linden, P.J.; Glatzel, P.; Lapras, C.; Krzyzowski, M. Continuous Flow Cryostat for X-Ray Fluorescence. *AIP Conf. Proc.* **2010**, *1234,* 617-620.

[57] Boesenberg, U.; Ryan, C.G.; Kirkham, R.; Siddons, D.P.; Alfeld, M.; Garrevoet, J., Núñez, T.; Claussen, T.; Kracht, T.; Falkenberg, G. Fast X-ray microfluorescence imaging with submicrometer-resolution integrating a Maia detector at beamline P06 at PETRA III. *J. Synchrotron Radiat.* **2016**, *23*, 1550-1560.

TOC

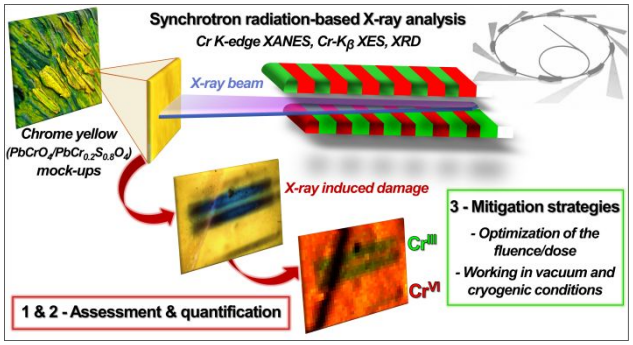

For Table of Contents Only

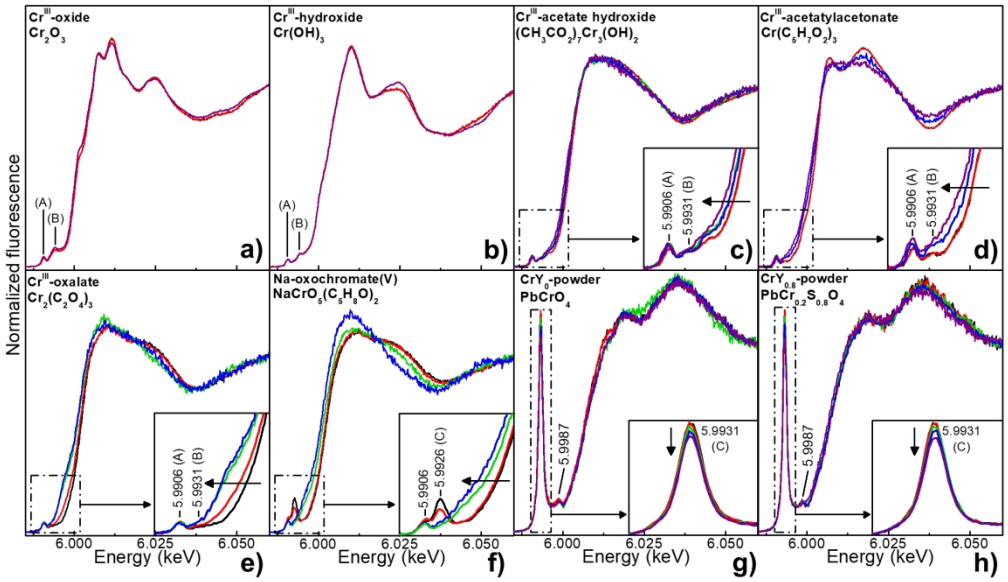

Figure 1. Cr K-edge XANES spectra of Cr-powders acquired at increasing fluences/doses at ESRF-ID21: (a) Cr^{III}-oxide, (b) Cr^{III}-hydroxide, (c) Cr^{III}-acetate hydroxide, (d) Cr^{III}-acetylacetonate, (e) Cr^{III}-oxalate, (f) Na-oxochromate(V), (g) CrY_0-powder, (h) $CrY_{0.8}$-powder [black: 1.7×10^7 ph/μm^2 (0.1-0.6 MGy); red: 1.7×10^8 ph/μm^2 (1-6 MGy); green: ~5.7×10^{11} ph/μm^2 (~5×10^3-2×10^4 MGy); blue:1-2×10^{12} ph/μm^2 (~9×10^3-4×10^4 MGy); purple: 1-2×10^{13} ph/μm^2 (~2-4×10^5 MGy)].

170x98mm (300 x 300 DPI)

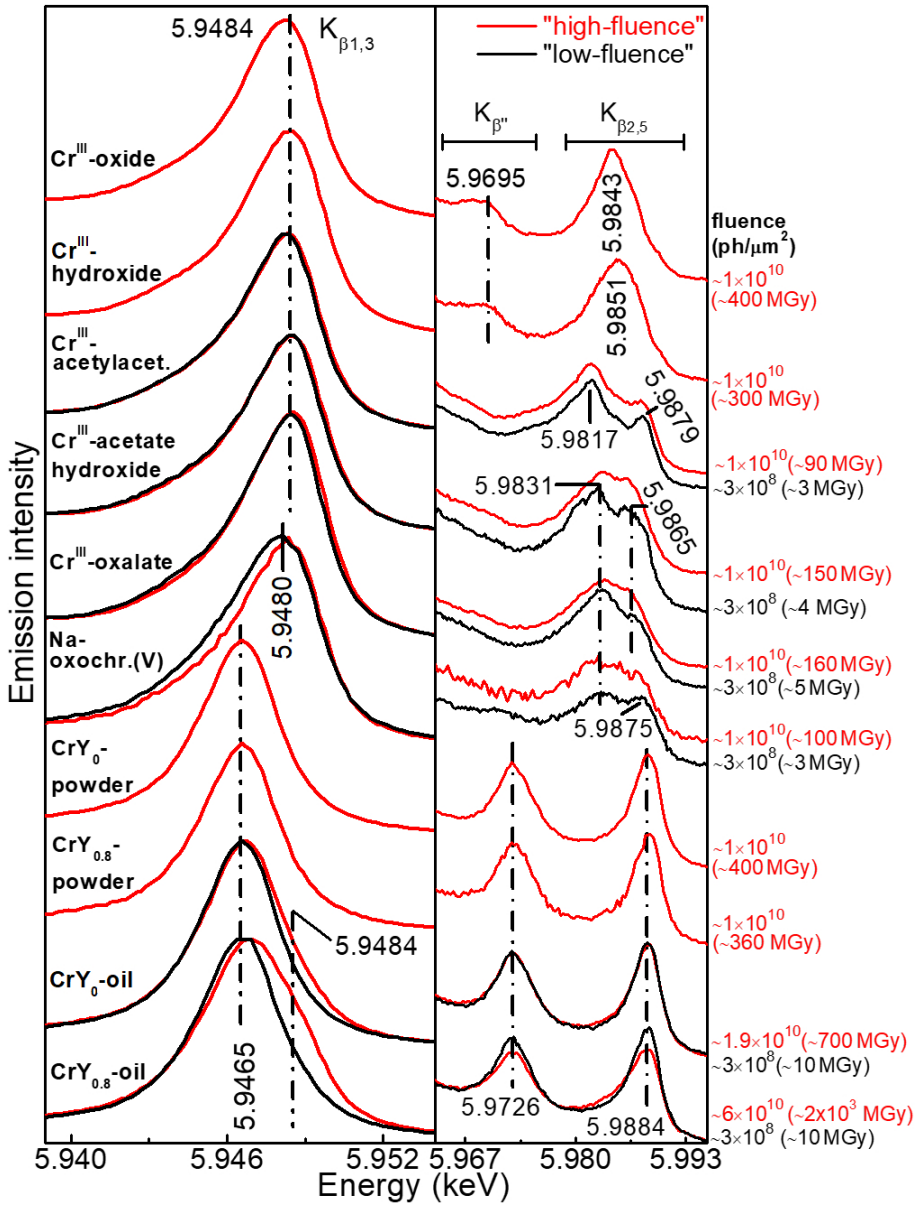

Figure 2. Cr-K_β XES spectra of Cr-samples recorded using "high-fluence" (red) and "low-fluence" (black) conditions at ESRF-ID26: (left) $K_{\beta 1,3}$ line; (right) K_β satellite lines (see Figure S3 for the complete spectra of K_β main lines). Fluences along with absorbed doses (in brackets) are also reported.

85x112mm (300 x 300 DPI)

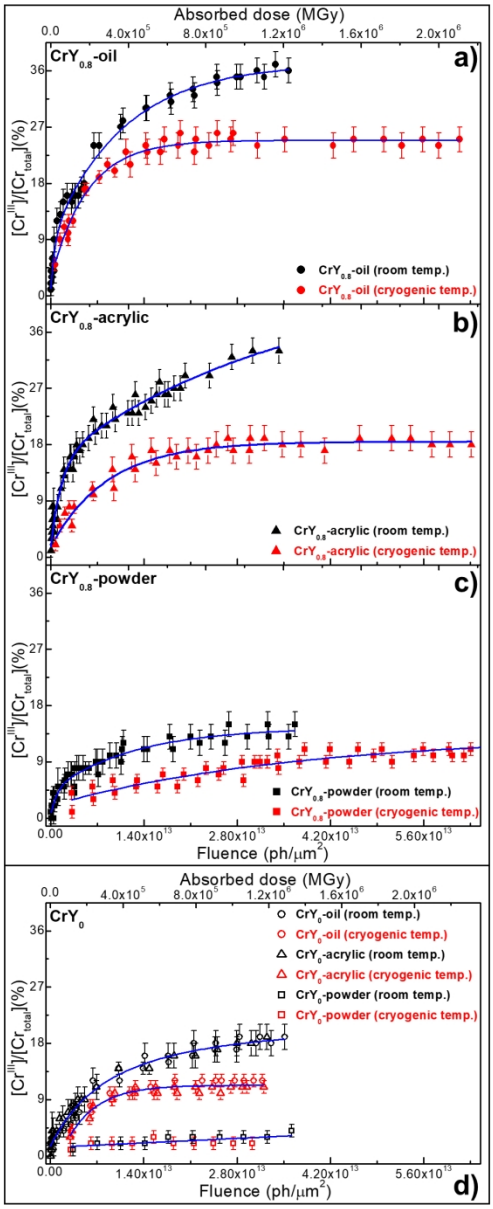

Figure 3. Plots of Cr^{III}-relative amount percentage *vs.* fluence/absorbed dose obtained at room temperature (black) and cryogenic temperature (red) at ESRF-ID21: (a-c) $CrY_{0.8}$-samples; (d) CrY_0-samples. In blue, fit obtained using mono-exponential or bi-exponential functions.

85x209mm (300 x 300 DPI)

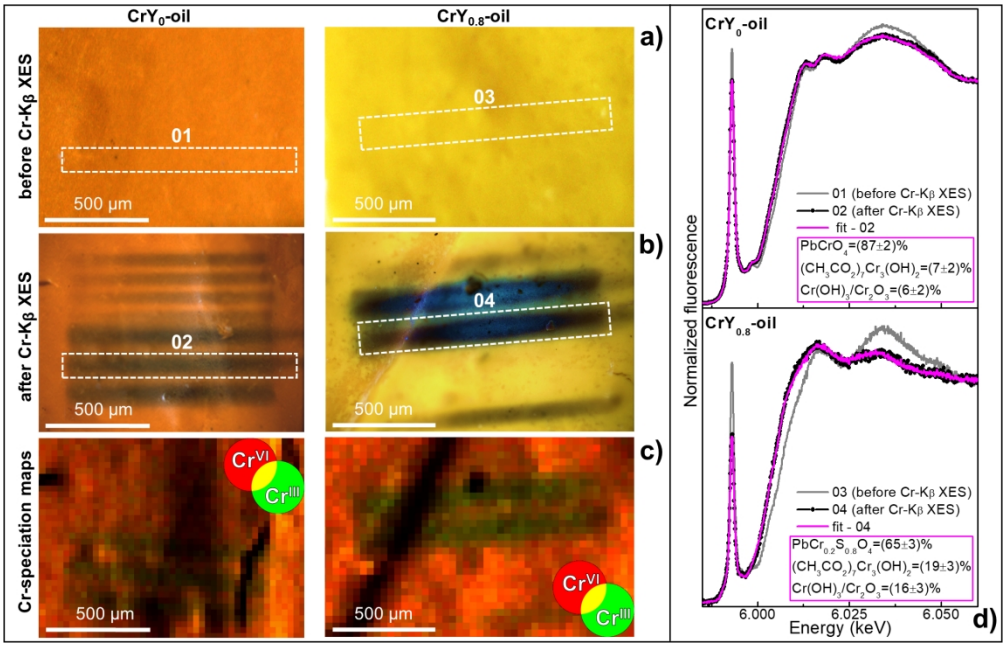

Figure 4. Photomicrographs of CrY_0-oil and $CrY_{0.8}$-oil (a) before and (b) after "high-fluence" Cr-Kβ XES investigations (*cf.* Figure 2 for the corresponding XES spectra). (c) RG composite SR µ-XRF Cr^{VI}/Cr^{III} maps recorded from the areas shown in (b) at ESRF-ID21 [step size (h×v): 30×30 µm^2; exp. time: 100 ms/pixel]. (d) Cr K-edge XANES spectra (grey and black) recorded at ESRF-ID26 from the regions shown by the rectangles in (a,b) and corresponding LCF results (magenta).

180x115mm (300 x 300 DPI)

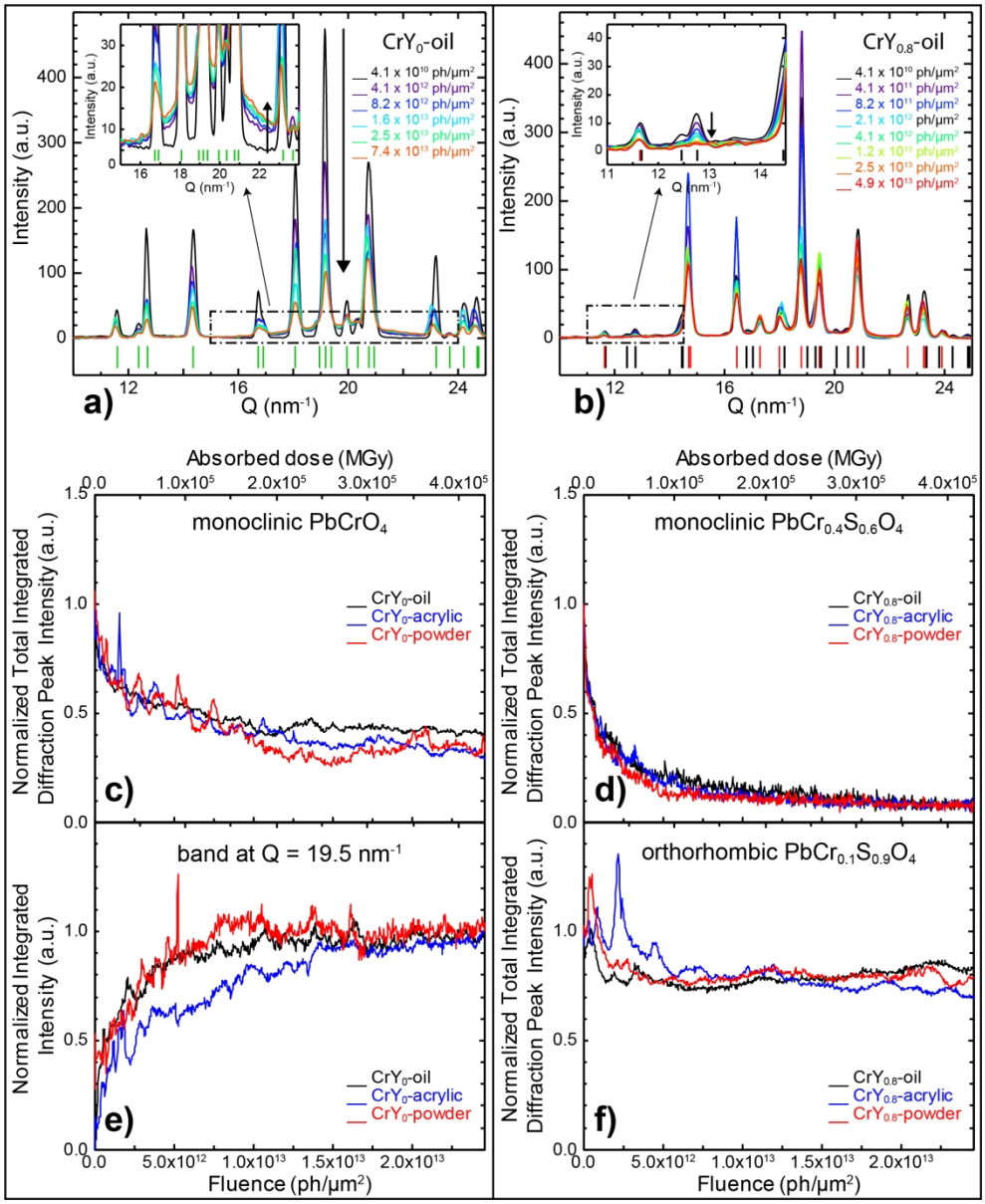

Figure 5. µ-XRD patterns collected from (a) CrY_0-oil and (b) $CrY_{0.8}$-oil at increasing fluences/doses at DESY-P06. Vertical bars indicate the diffraction peak positions of monoclinic $PbCrO_4$ (green), monoclinic $PbCr_{0.4}S_{0.6}O_4$ (black) and orthorhombic $PbCr_{0.1}S_{0.9}O_4$ (red). Normalized integrated intensity *vs.* fluence/absorbed dose of (c) monoclinic $PbCrO_4$, (d) monoclinic $PbCr_{0.4}S_{0.6}O_4$, (e) amorphous phase and (f) orthorhombic $PbCr_{0.1}S_{0.9}O_4$ in CrY_0-/$CrY_{0.8}$-samples (black=oil; blue=acrylic; red=powder).

178x217mm (299 x 299 DPI)

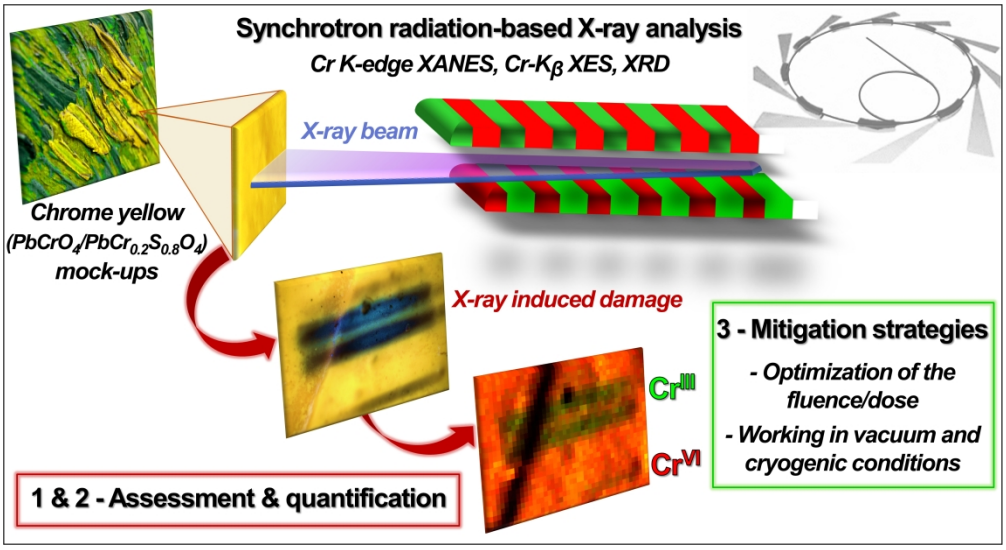

Table of Contents

331x178mm (300 x 300 DPI)